Evaluation of δ-Phase $ZrH_{1.4}$ to $ZrH_{1.7}$ Thermal Neutron Scattering Laws Using Ab Initio Molecular Dynamics Simulations

Mehta, Vedant; Rehn, Daniel; Olsson, Pär

Published in:
Journal of Nuclear Engineering

DOI:
10.3390/jne5030022

2024

Document Version:
Publisher's PDF, also known as Version of record

Journal of
Nuclear Engineering

MDPI

Article

Evaluation of δ-Phase $ZrH_{1.4}$ to $ZrH_{1.7}$ Thermal Neutron Scattering Laws Using Ab Initio Molecular Dynamics Simulations

Vedant K. Mehta [1], Daniel A. Rehn [2,*] and Pär A. T. Olsson [3,4]

[1] Nuclear Engineering and Nonproliferation Division, Los Alamos National Laboratory, Los Alamos, NM 87545, USA
[2] Computational Physics Division, Los Alamos National Laboratory, Los Alamos, NM 87545, USA
[3] Department of Materials Science and Applied Mathematics, Malmö University, SE-205 06 Malmö, Sweden
[4] Division of Mechanics, Materials and Component Design, Lund University, P.O. Box 118, SE-221 00 Lund, Sweden
* Correspondence: rehnd@lanl.gov

Abstract: Zirconium hydride is commonly used for next-generation reactor designs due to its excellent hydrogen retention capacity at temperatures below 1000 K. These types of reactors operate at thermal neutron energies and require accurate representation of thermal scattering laws (TSLs) to optimize moderator performance and evaluate the safety indicators for reactor design. In this work, we present an atomic-scale representation of sub-stoichiometric ZrH_{2-x} ($0.3 \leq x \leq 0.6$), which relies on ab initio molecular dynamics (AIMD) in tandem with velocity auto-correlation (VAC) analysis to generate phonon density of states (DOS) for TSL development. The novel NJOY+NCrystal tool, developed by the European Spallation Source community, was utilized to generate the TSL formulations in the A Compact ENDF (ACE) format for its utility in neutron transport software. First, stoichiometric zirconium hydride cross sections were benchmarked with experiments. Then sub-stoichiometric zirconium hydride TSLs were developed. Significant deviations were observed between the new δ-phase ZrH_{2-x} TSLs and the TSLs in the current ENDF release. It was also observed that varying the hydrogen vacancy defect concentration and sites did not cause as significant a change in the TSLs (e.g., $ZrH_{1.4}$ vs. $ZrH_{1.7}$) as was caused by the lattice transformation from ϵ- to δ-phase.

Keywords: thermal scattering law; $S(\alpha,\beta)$; zirconium hydride; NJOY; NCrystal

check for updates

Citation: Mehta, V.K.; Rehn, D.A.; Olsson, P.A.T. Evaluation of δ-Phase $ZrH_{1.4}$ to $ZrH_{1.7}$ Thermal Neutron Scattering Laws Using Ab Initio Molecular Dynamics Simulations. *J. Nucl. Eng.* **2024**, *5*, 330–346. https://doi.org/10.3390/jne5030022

Academic Editor: Dan Gabriel Cacuci

Received: 5 March 2024
Revised: 31 July 2024
Accepted: 13 August 2024
Published: 13 September 2024

1. Introduction

Special-purpose reactor concepts are next-generation advanced fission concepts with thermal power output between 1 kWe and 10 MWe. Their key features are (i) transportable, (ii) compact, and (iii) self-regulating for either solo remote or hybrid with renewable applications. A similar highly enriched uranium (HEU) reactor in this category, the Kilowatt Reactor Using Stirling TechnologY (KRUSTY), concluded its testing in March 2018 at the Nevada National Security Site (NNSS) [1–8]. Due to its use of HEU material, KRUSTY operated in the fast energy spectrum. For civilian or commercial applications, the special purpose concepts need to utilize non-HEU concepts, such as low-enriched uranium (LEU) or high-assay low-enriched uranium (HALEU) fuel (<19.75 at% ^{235}U). Reducing the enrichment level, and thus the overall ^{235}U fissile material, typically results in a decrease in the overall reactivity in the core. One way to overcome this is to soften the neutron energy spectrum by introducing high hydrogen density moderators, such as zirconium hydride or yttrium hydride, to increase the neutron capture probability in ^{235}U [9] and achieve a critical configuration.

Figure 1 shows the hydrogen atom density in various elements as a function of temperature. In addition to retaining most of the hydrogen at intermediate temperatures (800 K to 1000 K), ZrH_{2-x} also provides excellent neutronic properties due to the low absorption cross section of Zr at thermal energies. Hydrogen dissociation causes a rapid decrease in the hydrogen density at high temperatures. This could cause an issue for reliable reactor operation, and thus

the use of the ZrH moderator is limited to less than 1000 K. Specific examples of ZrH use in reactor systems over the past several decades, either as a heterogenous moderator material or a homogenous material with the fuel, were demonstrated in the Soviet Topaz reactors [10] or the TRIGA [11] and SNAP reactors in the U.S. [9,12]. Current designs, such as the nuclear thermal propulsion (NTP) [13] and MARVEL programs [14], also utilize zirconium hydride for neutron moderation. ZrH_{2-x} exists in the stable δ configuration for stoichiometries between $1.56 \leq H/Zr \leq 1.64$, as shown in Figure 2. Inside a reactor core, the temperature deviation (ΔT) in the metal hydride moderators can cause local changes in hydrogen concentration driven by hydrogen migration [9,15]. This results in hydrogen relocation and local changes in hydride stoichiometry (H/Zr). This phenomenon was experimentally observed by Trellue et al. [16] for an yttrium hydride system. Similarly, for ZrH, an initial $(H/Zr)_0$ stoichiometry can evolve into $(H/Zr)_0 \pm \Delta$, where the value of Δ is primarily determined by the thermodynamics of ZrH_{2-x} (internal physics) and the temperature gradient within the material (external loading). This requires the refinement of thermal scattering laws (TSLs or $S(\alpha, \beta)$) for the stable region of interest for nuclear reactors (Figure 2), i.e., the δ-phase in the range $ZrH_{1.4}$ to $ZrH_{1.7}$.

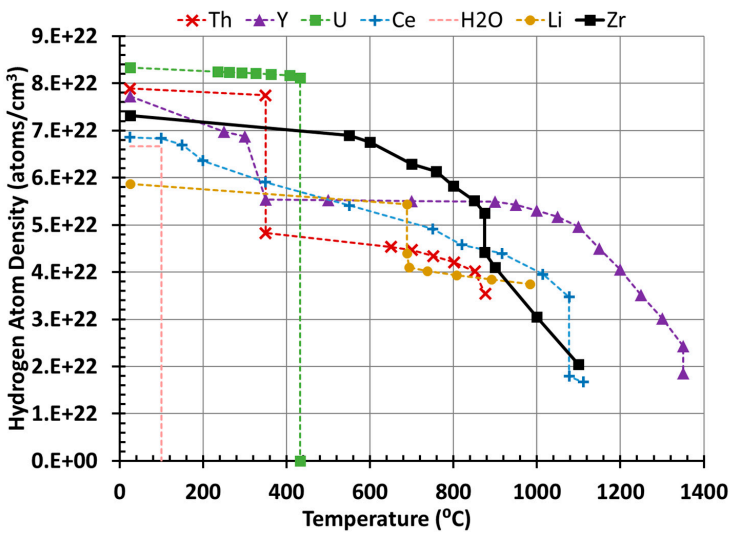

Figure 1. Hydrogen atom density in various metal–hydrogen systems as function of temperature in equilibrium with 1 atm hydrogen gas (from [17], based on the data from references listed therein).

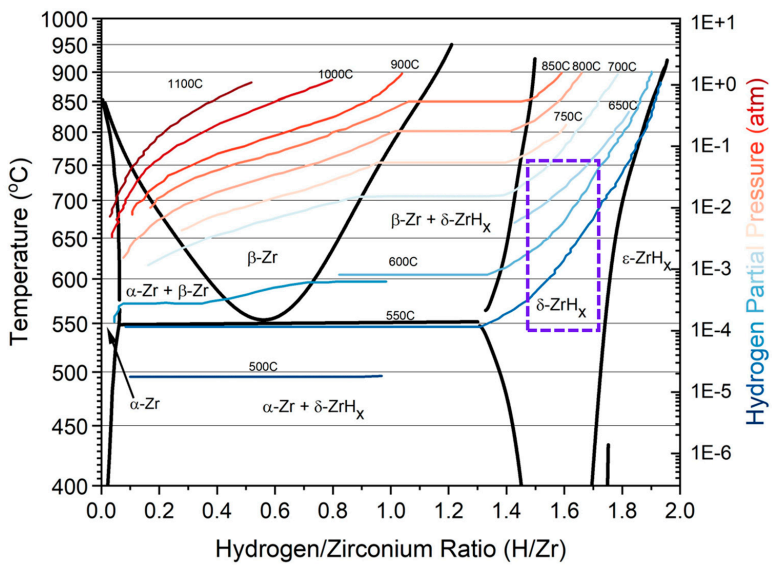

Figure 2. Zr-H phase diagram with PCT curves. (from [18,19], based on the data from references listed therein). The dashed line box represents potential steady state reactor operation regime.

In recent years, several initiatives [20–23] have been carried out by international researchers to provide a more accurate representation of zirconium hydride TSLs using first-principles atomistic methods. For instance, in the seminal work by Wormald et al. [20], ab initio lattice dynamics (AILD) and ab initio molecular dynamics (AIMD) in conjunction with velocity-autocorrelation (VAC) analyses were used to generate phonon density of states (DOS) and subsequently TSLs for δ-$ZrH_{1.5}$ and ϵ-ZrH_2. This work extends the work of Wormald et al. [20] and focuses more on δ-phase ZrH at intervals of H/Zr between 0.05 and 0.1. While AILD rely on computing the force constants associated with small displacements to construct the dynamical matrix, the AIMD approach is used to monitor the vibrational motion, where the phonon DOS is obtained through the Fourier transform of the VAC function. The previous study noted that the hydrogen phonon DOS computed by means of AILD resulted in a high frequency spectrum compared to experimental data, while the hydrogen phonon DOS computed using AIMD and VAC led to more consistent results [20]. Their calculation method included a coherent elastic component due to the use of a North Carolina State University solver named Full Law Analysis Scattering System Hub (FLASSH) [24]. Zu et al. [21] performed similar analyses to create δ-$ZrH_{1.5}$ and ϵ-ZrH_2 phonon DOS, but to compute the force constants, they adopted an AILD approach based on density functional perturbation theory (DFPT [25]), using the ab initio calculator VASP [26,27] combined with the PHONOPY pre- and post-processing tool [28,29]. They used a nuclear data processing code, NECP-Atlas [30], for their TSL evaluations and ignored the coherent elastic scattering component, as is the norm in hydrogen-bound systems. El Barbari et al. [22] added a third fcc phase, δ-ZrH_2, in addition to the aforementioned two crystal structures, to their phonon DOS calculations based on the DFPT method as implemented in the ABINIT software [31]. However, their calculations were performed using an exchange-correlation description formulated within the local density approximation, which is generally considered to be a less accurate approximation than the generalized gradient approximation (GGA) commonly used in the literature. For the TSL calculations, they used the industry standard Los Alamos National Laboratory code NJOY2016 [32], which is limited to a hydrogen-dominated incoherent approximation and ignores the coherent elastic component in zirconium. Finally, more recently, Švajger et al. [23] created phonon DOS for ϵ-ZrH_2 using VASP with GGA and compared it with experimental results; however, they did not report any TSL evaluations.

There are two main takeaways from the available literature. First, the non-symmetric/sub-stoichiometric δ-phase ZrH_{2-x} phonon DOS have yet to be evaluated, which limits the ability to account for environmentally induced localized hydrogen-concentration variations on the neutron thermal scattering properties. For instance, if an incorporated $ZrH_{1.6}$ moderator in a reactor evolves into a $ZrH_{1.55}$-$ZrH_{1.65}$ profile due to thermal diffusion (as detailed in [15]), the existing evaluations may have limited ability to predict the impact of hydrogen diffusion on neutronics. Second, the coherent elastic component is typically overlooked during TSL calculations due to the dominance of hydrogen incoherence.

To overcome these issues, first we evaluate the phonon DOS for the following sub-stoichiometric non-symmetric configurations: δ-$ZrH_{1.4}$, δ-$ZrH_{1.5}$, δ-$ZrH_{1.55}$, δ-$ZrH_{1.6}$, δ-$ZrH_{1.65}$, and δ-$ZrH_{1.7}$, along with the stoichiometric ϵ-ZrH_2. To this end, we adopted the approach outlined in [20], which relies on AIMD in tandem with VAC analysis. While the emphasis of this study is on the δ-phase, we study the ϵ-phase to validate the methodology with available data in the literature. Second, to account for the coherent scattering component in our calculations, in this study we use the novel toolkit NJOY+NCrystal [33] developed by the European Spallation Source. This tool allows computation of both coherent and incoherent elastic components and stores them in the ACE format for their utility in neutron transport solvers such as MCNP® [34]. Another key advantage of this tool is that it allows for the definition of site occupancy factors (SOF) using an @ATOMDB flag to account for defects and impurities in a crystal. The selected ZrH_{2-x} configurations will allow for higher-fidelity reactor physics calculations and also account for variations in stoichiometry after hydrogen diffusion.

2. Computational Methods

In the present section, we detail the procedures to generate the ab initio phonon data and the TSLs. As part of the former, we also describe the approach to generate and select representative sub-stoichiometric hydride configurations that were used for the phonon calculations.

2.1. Atomic Scale Simulations

For the non-stoichiometric cubic δ-ZrH_{2-x} phase, Zr atoms are positioned at the regular fcc-sites, and the hydrogen randomly occupies tetrahedral interstitial sites [19]. To generate realistic configurations, we created supercells that were based on the primitive fcc cell. The size of the supercells was carefully converged with respect to the hydrogen phonon DOS, which revealed that a supercell of a $4 \times 4 \times 4$ grid of primitive fcc cells was sufficient to yield well-converged results. Thus, systems containing 64 Zr and up to 109 H atoms were considered for the sub-stoichiometric δ-phase.

To create configurations with random H occupancy, all tetrahedral interstitial sites were initially occupied by H atoms, after which a set was randomly selected and removed to match the target stoichiometry. For each degree of hydrogen content, we created 15 configurations with different random H occupancy that were fully relaxed, i.e., both coordinates and cells. This enabled the configurations to relax to assume the shape of non-cubic crystals if such transformation was induced as a result of the random hydrogen occupancy. Among the 15 relaxed configurations, those that were chosen for the subsequent DFT modelling were the ones that exhibited the lowest ground state energy and maintained close to cubic symmetry. The latter was evaluated based on the resulting supercell vectors following relaxation, where we considered the crystal to be cubic if the change in angle was less than 1° and the size difference between the largest and smallest vectors was less than 0.5%. In Figure 3, we illustrate the representative configuration for $ZrH_{1.6}$ and the hydrogen concentration-dependent lattice parameter. Although the difference in lattice parameter increases with increasing hydrogen content, the largest observed discrepancy between DFT and experimental data is of the order of 0.015 Å, which suggests a good agreement.

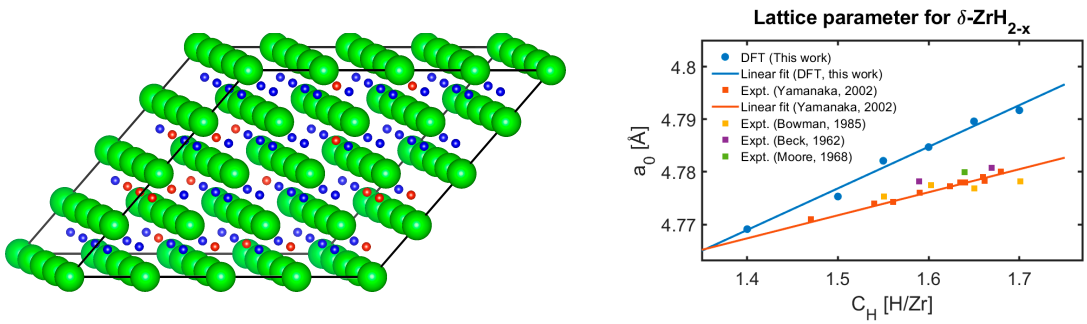

Figure 3. (**Left**) The non-stoichiometric $ZrH_{1.6}$ phase with random hydrogen occupancy used in the AIMD simulations. The green and blue atoms correspond to Zr and H, respectively, while the red spheres indicate random vacant H sites. (**Right**) Hydrogen concentration-dependent lattice parameter compared with experimental data [35–38].

Phonon DOS constitute the most fundamental input data for generating TSLs. The two most common approaches to extract the phonon DOS from first principles modelling entail: (i) computing the force constants associated with small displacements and diagonalizing the dynamical matrix, i.e., the AILD approach (see, e.g., [24,28,29,39,40]), and (ii) Fourier transforming the VAC obtained from AIMD simulations [41]. Both of these approaches have been previously used to generate phonon DOS for TSLs; see, e.g., [42,43]. Since the former typically exploits crystal symmetries, which can reduce the computational effort substantially, it tends to be preferred for ordered crystals or alloys. However, for non-stoichiometric systems with random occupancy, such as those considered herein, much of the symmetry is lost, and therefore the number of independent displacements and

numerical cost can, in general, not be reduced. In addition, as discussed in [20], AIMD overcomes several shortcomings of the AILD approach: Because the AILD approach relies exclusively on small displacements, anharmonic effects are not effectively accounted for. But because of its low mass, H is expected to experience significant dynamics at a finite temperature, which may trigger anharmonic contributions and lead to broadening of the phonon DOS. Therefore, because anharmonicity is naturally incorporated in the AIMD VAC analysis, we opted to use this approach for this study.

All DFT modelling in this work was conducted using VASP (version 5.4.4) [26,27], which is a plane-wave-based DFT package. We tested different projector-augmented wave (PAW) potentials [44,45], but chose to use GW-type PAW potentials with the electronic valence configurations given by $4s^2 4p^6 5s^1 4d^3$ and $1s^1$ for Zr and H to represent the core states, respectively. This choice was mainly motivated by the fact that it resulted in a slightly improved consistency with experimental data in terms of lattice parameters for different hydrogen contents (see Figure 3). We used the Perdew–Burke–Ernzerhof (PBE) GGA [46] for the exchange-correlation functional. For the static supercell simulations, we used a plane wave energy cutoff of 525 eV and a Γ-centered Monkhorst-Pack k-point grid of $2 \times 2 \times 2$ [47], of which the former was reduced to 350 eV for the AIMD simulations. Although the latter is just slightly higher than the minimum recommended cutoff, we performed a force convergence study for a set of configurations that were subjected to randomized displacements such that the magnitude of the force components ranged from 2 meV/Å to approximately 4 eV/Å. It revealed that the root mean square error of the force components was approximately 8 meV/Å when comparing the forces associated with the 350 eV cutoff with those of 500 eV. This level of force convergence is expected to yield sufficiently accurate trajectories for the AIMD simulations to give a good representation of the phonon DOS.

The AIMD simulations were performed at 300 K, for which we adopted a two-step procedure. In the first step, equilibration of the system was achieved by performing AIMD modelling within the NVT ensemble using a Nosé-Hoover thermostat [48–51]. These simulations were allowed to run for 1 ps, using a time integration step of 0.25 fs. To facilitate the equilibration procedure, the atoms were initially slightly displaced to emulate the canonical ensemble using the TDEP software (version 1.1) [52–54]. The equilibration was followed by NVE dynamics for an additional 1.5 ps, during which the velocities were recorded at every timestep, such that the phonon DOS could subsequently be computed as the Fourier transformation of the VAC function. To account for the thermal expansion of the relaxed structures at 0 K to 300 K, during the NVE simulations of the second part of the simulation, we monitored the pressure and used linear elasticity theory based on the elastic constants in [55] to isotropically expand the supercell vectors such that the resulting pressure magnitude was reduced to below 200 MPa. Following this adjustment, we repeated the NVT and NVE simulations with the updated supercell to recompute the corrected phonon DOS.

2.2. Thermal Scattering Law or S(α,β)

At thermal neutron energies (<2 eV), the free gas assumption for neutron interactions with the crystal is no longer valid. This is because the lattice binding or structure determines how the incoming thermal neutron will be distributed into an exit scattering angle and energy. The scattering function $S(\alpha, \beta)$ is used to describe the crystal-binding effects of a particular material. The double-differential scattering cross section for thermal neutrons interacting with a bound system [40,56–60] is defined as:

$$\sigma(E \to E', \mu) = \frac{\sigma_{coh} + \sigma_{inc}}{2k_B T} \sqrt{\frac{E'}{E}} S(\alpha, \beta), \tag{1}$$

where E and E' are the incident and scattered neutron energies, respectively; μ is defined as the cosine of the scattering angle in the laboratory system; k_B is the Boltzmann constant; T is the temperature of the material; σ_{coh} and σ_{inc} are the coherent and incoherent terms of the bound atom scattering cross section, respectively; and S is the scattering function, also

known as the asymmetric TSL. Note that the TSL is a function of only two temperature-dependent terms: (i) the dimensionless momentum transfer α and (ii) the dimensionless energy transfer β. The momentum transfer term is defined as:

$$\alpha = \frac{E' + E - 2\mu\sqrt{E'E}}{Ak_BT}, \tag{2}$$

where A is the ratio of the scatterer mass to the neutron mass. The energy transfer term is defined as

$$\beta = \frac{E' - E}{k_BT}. \tag{3}$$

The TSL can be further broken down as follows:

$$S(\alpha, \beta) = S_d(\alpha, \beta) + S_s(\alpha, \beta), \tag{4}$$

where the S_d is the distinct (d) events from the scattering wave interference arising from the different scattering zones, and S_s is the self (s) scattering event, which excludes the interference. For crystal bound systems, the harmonic assumption allows the TSL to be expressed according to the phonon expansion model as follows:

$$S(\alpha, \beta) = \sum_{n=0}^{\infty} S^n(\alpha, \beta), \tag{5}$$

where n is the number of phonons excited or deexcited during the neutron scattering event with the material. Increasing n represents an increase in the order of convolution for the phonon spectra. This expansion represents the zero-term as the elastic component, whereas the non-zero terms constitute the inelastic component. For polycrystalline solids, distinct wave interference is typically neglected for the inelastic scattering resulting in an incoherent approximation [40,57]. Using all the above information, the double-differential scattering cross section can be rewritten as:

$$\sigma(E \to E', \mu) = \frac{1}{2k_BT}\sqrt{\frac{E'}{E}}\left(\sigma_{coh}\left(S_d^0(\alpha, \beta) + S_s^0(\alpha, \beta) + \sum_{n=1}^{\infty} S_s^n(\alpha, \beta)\right) + \sigma_{inc}\left(S_s^0(\alpha, \beta) + \sum_{n=1}^{\infty} S_s^n(\alpha, \beta)\right)\right). \tag{6}$$

where the coherent and incoherent scattering cross section can be decomposed into elastic and inelastic components.

For H bound in ZrH_{2-x}, the incoherent approximation is applied and interference is neglected. Since S becomes S_s, the double differential cross section for inelastic scattering (σ_{in}) can now be expressed as:

$$\sigma_{in}(E \to E', \mu) = \frac{\sigma_{coh} + \sigma_{inc}}{2k_BT}\sqrt{\frac{E'}{E}}\sum_{n=1}^{\infty} S_s^n(\alpha, \beta), \tag{7}$$

where the self-scattering TSL is written as:

$$S_s^n(\alpha, \beta) = \frac{1}{2\pi}\int_{-\infty}^{\infty} e^{i\beta t}e^{-\gamma(t)} \times \frac{1}{n!}\left(\alpha\int_{-\infty}^{\infty} \frac{\rho(\beta)}{2\beta\sinh(\beta/2)}e^{-\beta/2}e^{-i\beta t}d\beta\right)^n dt, \tag{8}$$

where t is time and the function $\gamma(t)$ is calculated as

$$\gamma(t) = \alpha\int_{-\infty}^{\infty} \frac{\rho(\beta)}{2\beta\sinh(\beta/2)}\left[1 - e^{-i\beta t}\right]e^{-\beta/2}d\beta. \tag{9}$$

In the above two equations, $\rho(\beta)$ is the phonon DOS evaluated by the atomistics or experimental methods as discussed earlier. During TSL evaluations, the phonon frequency spectrum is normalized to unity.

ENDF/B-VIII.0 [58]—short for Evaluated Nuclear Data Library—is the United States' default neutron and other particle database regularly used in particle transport codes such as MCNP and SCALE. In the latest ENDF/B-VIII.0 release, Zr bound in ZrH and H bound in ZrH TSLs were both generated under the incoherent approximation limited by combination of the LEAPR module of NJOY [32] and ENDF formatting. Therefore, scattering from zirconium bound in the crystal structure (Bragg edges) was also neglected. Such approximations are typically valid, at least initially, and therefore are also applied to other metal–hydrogen-bound systems as well [59,60]; however, the coherent elastic scattering component ($\sigma_{coh} S_d^0$) arising from the distinct wave interference of the bonded metal is still absent. This was recently corrected and accounted for by Wormald et al. [20] for δ-$ZrH_{1.5}$ and ϵ-ZrH_2 TSLs and will also be applied in our work for the sub-stoichiometric configurations using NJOY+Ncrystal [33]. Ncrystal [61] contains well over 200 validated evaluations with support for both coherent and incoherent elastic components for solid crystalline materials, thus overcoming NJOY's six hard coded material limitations. This tool (i) implements changes to the original NJOY modules and provides an interface for extensive elastic component physics from Ncrystal to NJOY, and (ii) works around the current ENDF formatting limitations where the scattering is decomposed into individual elements for bound systems. The tool evaluates and sorts the contributions for a particular system and then distributes them across elements to satisfy ENDF formatting requirements. More details on Ncrystal can be found in the literature [61]. NJOY+Ncrystal will calculate the major elastic component and scale it to the total bound cross section for each atom. For the ZrH system, NJOY+Ncrystal will determine H as dominantly incoherent and apply the coherent elastic component ($\sigma_{coh} S_d^0$) to Zr, where Zr bound in ZrH_{2-x} is captured as:

$$\sigma(Zr\ in\ ZrH_{2-x}) = \sigma_{abs}^{Zr} + \sigma_{in}^{Zr} + \sigma_{el,coh}^{ZrH_{2-x}} \cdot \frac{\sigma_b^{Zr}}{\sigma_{b,coh}^{Zr}} \tag{10}$$

to satisfy the ENDF file format [62] and H bound in ZrH_{2-x} is captured as:

$$\sigma(H\ in\ ZrH_{2-x}) = (H/Zr) \cdot \left(\sigma_{abs}^{H} + \sigma_{in}^{H} + \sigma_{el,inc}^{H} \cdot \frac{\sigma_b^{H}}{\sigma_{b,inc}^{H}} \right) \tag{11}$$

to satisfy ENDF-6 format [62]. Note that the coherent component is a property of the crystal structure, whereas the incoherent component is a property of individual atoms. As such, without ENDF format restrictions, $\sigma_{el,coh}^{ZrH_{2-x}}$ should be applied to both elements. However, this ENDF formatting trick will provide sufficient resolution due to the dominance of the hydrogen incoherent component.

We recall that all the compositions of zirconium hydride are modeled using a single δ-phase structure; however, certain H/Zr compositions evaluated in this study can exist in two phases as shown in the phase diagram (Figure 2). For microreactor operating temperatures of 800–1000 K, the entire range from $ZrH_{1.4}$ to $ZrH_{1.7}$ exists in a single phase. In addition, particle transport codes such as MCNP permit only one TSL usage per nuclide for a given material. As such, a system where two TSLs are present to represent two distinct phases is precluded in MCNP. Henceforth, the study carried out here provides valuable information and insight on the TSL of zirconium hydride due to the changes in sub-stoichiometry.

3. Results and Discussion

3.1. Phonon DOS

In our modelling approach, we computed the phonon DOS using both AIMD and AILD for the widely studied stoichiometric ϵ-ZrH_2 phase and compared it with those computed by means of AILD elsewhere [55]. Moreover, we compared our results with those obtained for the hydrogen phonon DOS from inelastic neutron spectroscopy (INS) measurements [63,64] for both ϵ-ZrH_2 and δ-ZrH_{2-x}. We found that our AILD results

mostly agree with the results from [55], despite the fact that different PAW potentials and different exchange-correlation descriptions were used. Notable differences emerged for the acoustic band, where the lowest peak at approximately 15 meV is absent for the AIMD simulations. Below this energy level, the AIMD does not reproduce the expected square phonon DOS associated with the Debye model in the long-wave limit. As suggested in [43], we did increase the size of the supercell to that used in [20], which comprised $4 \times 4 \times 3$ unit cells (i.e., 96 Zr atoms and 192 H atoms). However, this did not lead to any significant improvement in the low-frequency DOS. Thus, even though we did not explore it any further herein, because of the significant computational cost for sub-stoichiometric configurations, one possibility would be to adopt the novel hybrid approach outlined in [20]. This entails extracting the low-frequency DOS from AILD and the hydrogen phonon DOS from AIMD. Nevertheless, even though the shapes of the acoustic band differ, they are located at similar points in the frequency spectrum with similar band widths. Above 15 meV, we find good agreement between AIMD and AILD phonon spectra (Figure 4). For two of the peaks, located at 20 and 25 meV, the AIMD results underestimate the AILD results by only 0.5 and 1.3 meV, respectively, highlighting the good agreement between the two different approaches above 15 meV.

The hydrogen band computed herein using the AILD method concurs well with that in [55]. The experimental results for the hydrogen phonon DOS vary slightly for different sources [63,64]. For the lower part of the hydrogen phonon DOS of ϵ-ZrH_2, we find that the results computed using AIMD are in good agreement with the results from [63], while the AILD is more in line with that in [64]. Notably, the AILD simulations predict a high peak at approx. 147 meV, which is much less pronounced and shifted to a slightly lower energy (approx. 145 meV) in the AIMD results. The latter peak position concurs well with experimental data [63,64] (see Figure 4). Although the AIMD phonon DOS is broader than that for AILD, we found that both modelling approaches produce the main features of experimental data [63,64] and are in reasonable agreement with experimental data. For the hydrogen phonon DOS of the sub-stoichiometric δ-ZrH_{2-x}, the computed AIMD-based data is in good agreement with the available experimental data in [63].

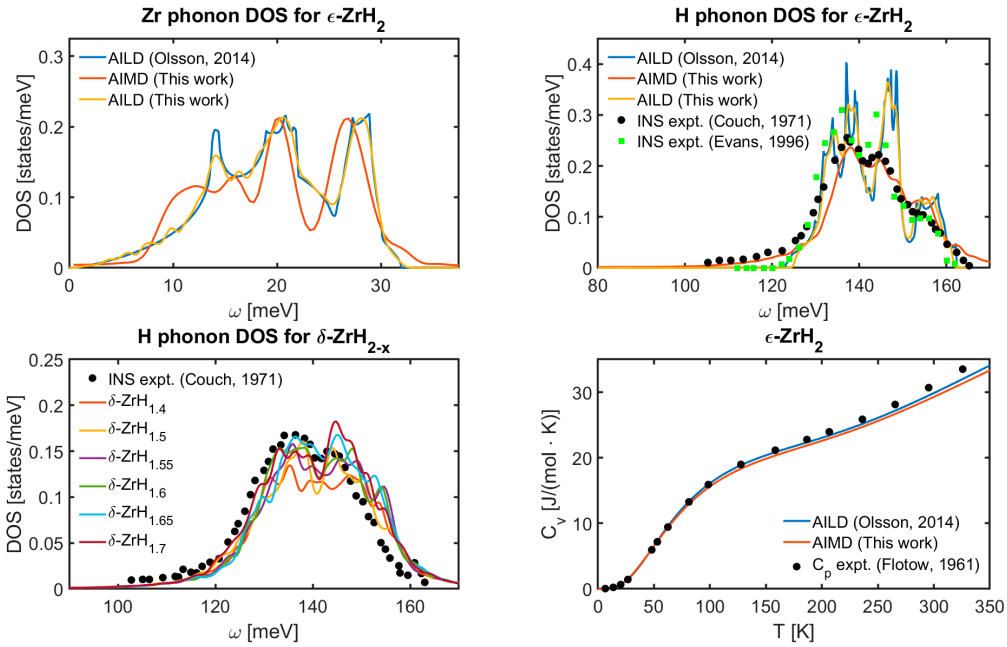

Figure 4. (**Top Left**) Phonon DOS for Zr and (**Top Right**) H in ϵ-ZrH_2. (**Bottom Left**) Hydrogen phonon density of states for sub-stoichiometric δ-ZrH_{2-x} computed using AIMD. The experimental data corresponds to $x = 0.44$. (**Bottom Right**) specific heat capacity for ϵ-ZrH_2. The experimental INS and heat capacity data are from [63–65] and the AILD data is from [55].

Moreover, we evaluated the specific heat capacity, C_v, for ϵ-ZrH_2, computed through the harmonic approximation against those performed in [55] and the experimental data of C_p from adiabatic calorimetry measurements in [65] up to room temperature. Figure 4 shows that both approaches provide almost identical results. While the computed curve using phonon data from [55] acts as an upper bound compared to the calculated data in this study, the difference between the two curves is less than 0.5 J/(mol·K) at room temperature, which corresponds to an upper limit deviation of about 2%. Our results underestimate the experimental data for two reasons. First, we did not account for the electronic contribution to the heat capacity in these calculations. This would correspond to about 0.5 J/(mol·K) at room temperature [55]. Second, because $C_p > C_v$, we should expect the value of C_v to be slightly lower than the experimental C_p data. However, our results capture the qualitative behaviour of the experimental data over the entire study range. The outcome of these benchmarks for the stoichiometric ϵ-ZrH_2 phase suggests that the adopted phonon modelling approach carried out in this study has good predictability, and thus we expect it to be transferable to consider non-stoichiometric phases.

3.2. Thermal Scattering Laws (TSLs)

3.2.1. Benchmark with the ENDF Evaluation

In the first part of our analysis, we perform (i) a verification with the current ENDF evaluation [58] and (ii) a validation with the experimental data [66,67] available in the literature; this is similar approach to Wormald et al.'s study [20]; see Figure 5. For verification, ZrH_2 phonon oscillations are in excellent agreement with the evaluation. Some discrepancies exist at lower energy, as the current ENDF evaluation ignores Bragg edges. In contrast, in this study, the Zr-bound TSLs contain these Bragg edges, giving rise to discrepancies from ENDF around these edges. Similarly, the generated TSLs are also in very good agreement with phonon oscillations and Bragg edges. However, the experimental Bragg cutoff seems to be slightly lower than the one modelled in our study. Similar observations were made by Wormald et al. [20]. In general, the generated stoichiometric TSLs show excellent correlation, allowing the analysis to be carried out on sub-stoichiometries.

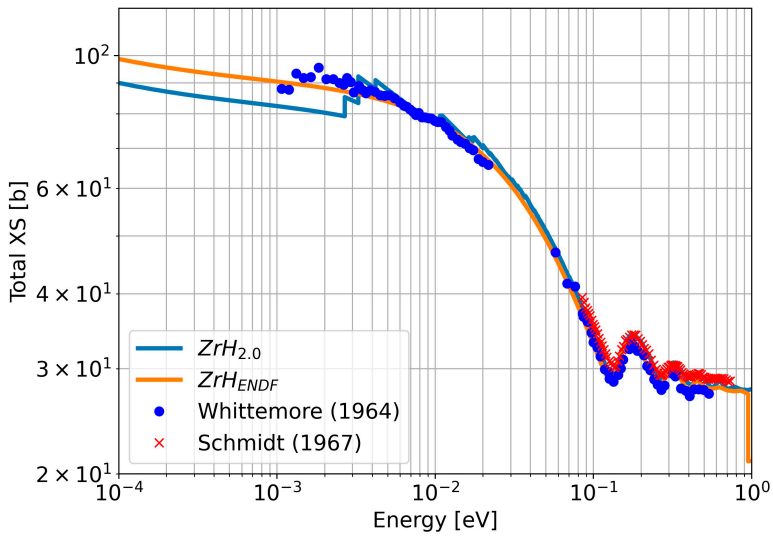

Figure 5. Verification and validation for the ϵ-ZrH_2 TSLs (this study) with ENDF evaluation [58] and experimental data [66,67].

3.2.2. New Evaluations

After achieving benchmark for stoichiometric TSLs, in this section, sub-stoichiometric TSLs were constructed using NJOY+Ncrystal [33] and Ncrystal [61] alone. Ncrystal allows for the most accurate evaluation of TSLs, whereas NJOY+Ncrystal allows the production of ACE files within the limitations of ENDF syntax. A comparison of TSLs for H/Zr ratios

between 1.4 and 1.7 with that of 2.0 is provided in Figure 6. On a per-average atom basis, δ-phase TSLs are closer to one another than the ϵ-phase TSL. The $1/v$ cross section seems to overlap for $1.5 \leq \mathrm{H/Zr} \leq 1.7$ as cross sections approach $1 \cdot 10^{-5}$ eV. ZrH_2 Bragg edges are noticeably different than ZrH_{2-x} due to change in phase. Detailed figures on elastic and inelastic components for all the sub-stoichiometric TSLs generated in this study are provided in Figure A1 of Appendix A.

These TSLs were then reconstructed into ACE files (Figure 7) using the NJOY+Ncrystal toolkit within the constraints of ENDF syntax as detailed in Section 2.2. ACE files distinguish between the individual contributions of each element in the crystal. The top panel shows the dominant contribution from each element, whereas the bottom panels show the total contribution of each element. Figure 7 compares the hydrogen inelastic component for the δ-phase and shows a trend of increasing cross section with decreasing H/Zr for $1.5 \leq \mathrm{H/Zr} \leq 1.7$. The cross section then decreases for $ZrH_{1.4}$, being closer to that of $ZrH_{1.6}$. There was no discernible trend in the $1/v$ region for the configurations as observed by Wormald et al. [20] between both phases. The NJOY+Ncrystal regenerates the optical phonon oscillations in the hydrogen component at a much lower resolution (Figure 7) than the Ncrystal alone (Figure 6). This lack of resolution was also observed in other metal–hydrogen systems and is thought to be related to a constraint in the THERMR module of NJOY, as initially observed by Zerkle and Holmes [59] for yttrium hydride. Figure 7 additionally emphasises that a coherent elastic contribution is captured in the Zr bound in the ZrH_{2-x} evaluation. Since the current ENDF ZrH TSL evaluation was constructed using NJOY's LEAPR module within the incoherent assumption, no Bragg edges were observed in the ENDF file. Figure 8 provides a comparison of total cross sections at 293 K and 1000 K. The TSL varies due to the vacancy defects but not as significantly as in other metal–hydrogen systems such as YH_x [60]. This could be explained due to the application of two different techniques, i.e., AIMD (this work) and AILD in [60]. However, these TSLs deviate significantly from the current ENDF release, thus proving their utility for high-fidelity neutronics modelling in the future.

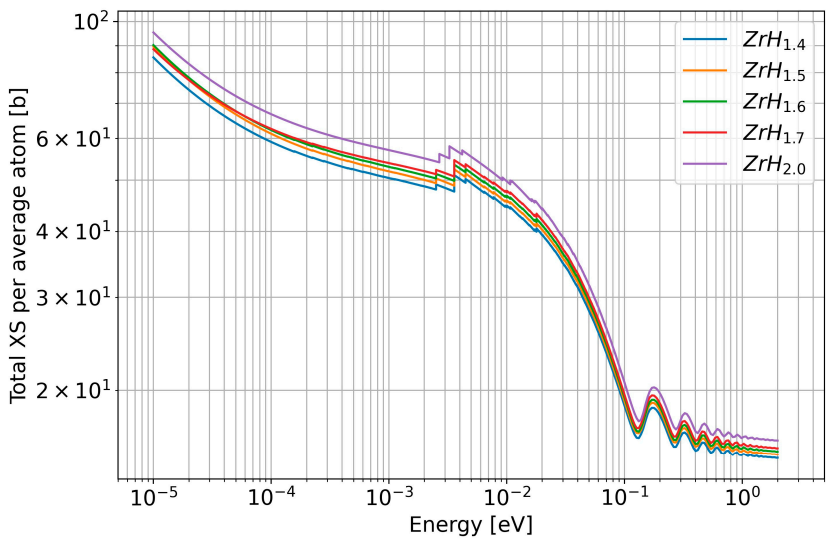

Figure 6. Cross sections for varying stoichiometries generated using Ncrystal. ZrH_2 is in the ϵ-phase.

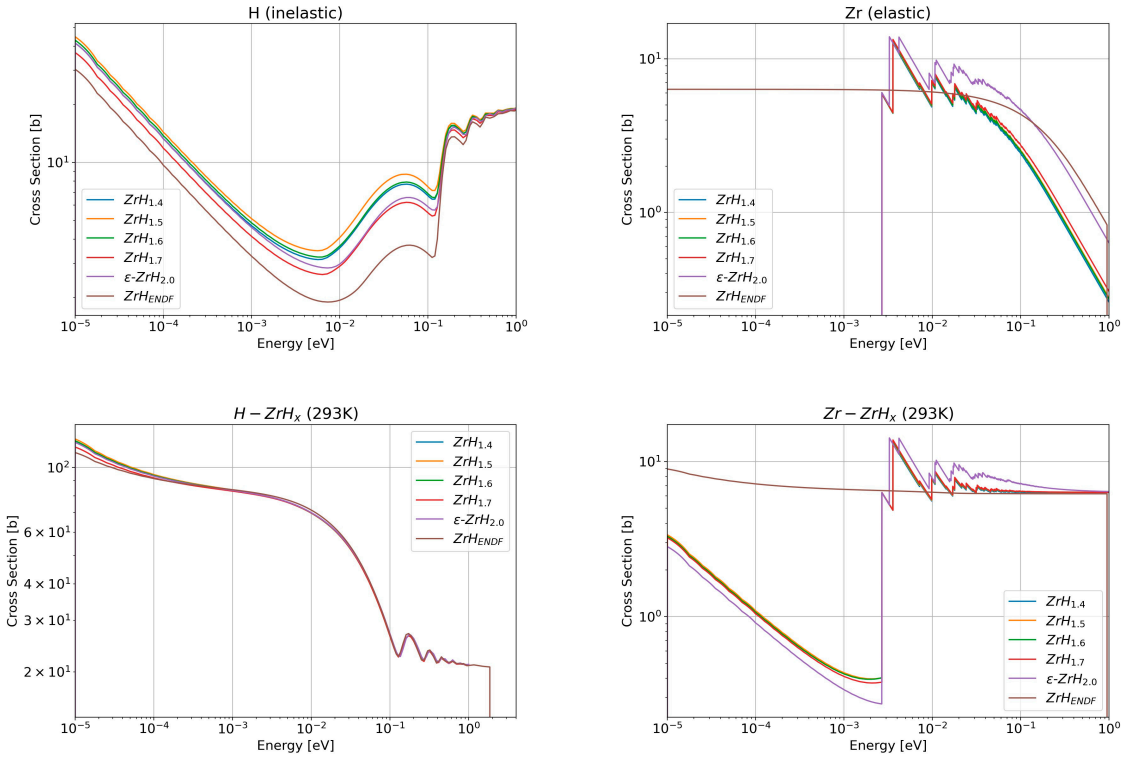

Figure 7. The hydrogen inelastic (**top left**) and zirconium elastic (**top right**) normalized ACE file components for room temperature. Along with total hydrogen bound in ZrH_{2-x} (**bottom left**) and zirconium bound in ZrH_{2-x} (**bottom right**) normalized ACE file TSLs compared with current ENDF release (in brown) [58]. The TSLs were generated using the NJOY+NCrystal software.

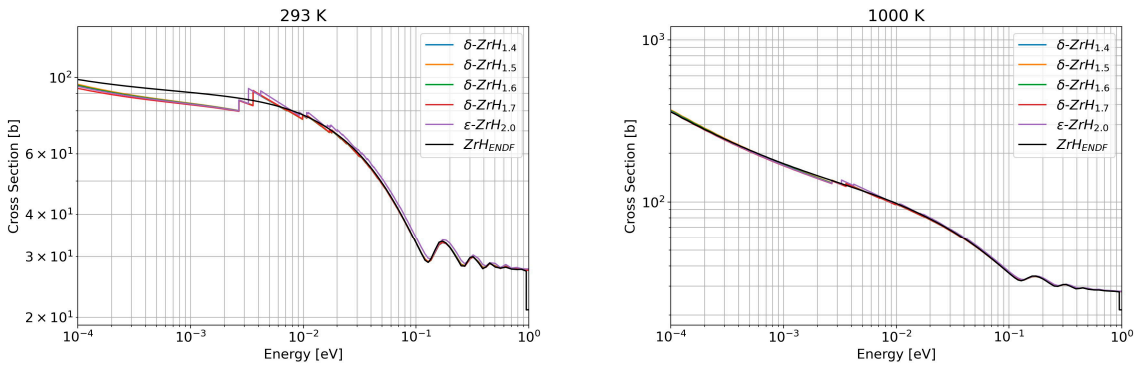

Figure 8. ACE cross section at 293 K (**left**) and 1000 K (**right)** for various ZrH_{2-x} sub-stoichiometries. The TSLs are plotted as $H(ZrH_{2-x})$ + $Zr(ZrH_{2-x})$ (instead of the total (H/Zr) $\times$ $H(ZrH_{2-x})$ + $Zr(ZrH_{2-x})$ cross section) for a normalized comparison.

4. Conclusions

In the present work, we developed TSLs for sub-stoichiometric δ-ZrH_{2-x} $(0.3 \leq x \leq 0.6)$ to explore how modifying stoichiometry affects behaviour. To this end, we adopted the approach outlined in [20], which used AIMD in conjunction with VAC to extract the phonon DOS. To mimic real material, the considered configurations consisted of cubic low-energy configurations with random hydrogen occupancy of the tetrahedral interstitial sites. The computed phonon DOS reproduced most of the experimentally observed features and those previously calculated using other techniques.

Even though phonons varied with vacancy defect concentration, the resulting TSLs did not deviate as much within the same δ-phase (i.e., $ZrH_{1.7}$ vs. $ZrH_{1.4}$). During the $\epsilon \rightarrow \delta$ phase transformation, larger deviations between the TSLs were observed. This

study also shows the high compatibility of the NJOY+NCrystal toolkit to generate TSLs for non-perfect crystals and its translation into the ENDF format. The coherent elastic and incoherent components of the cross section deviated significantly between the phases. Currently, the ENDF library contains only one type of ZrH_x TSL. This study directly allows the modelling of stoichiometries up to intervals of 0.1 H/Zr, eliminating the need for linear mixing of thermal treatments (as in [20]) for δ-phase zirconium hydride. This study provides an exact representation of sub-stoichiometric TSLs for higher-quality reactor modelling using neutron transport solvers such as MCNP®.

Author Contributions: Conceptualization: V.K.M., D.A.R. and P.A.T.O.; methodology: V.K.M., D.A.R. and P.A.T.O.; software: V.K.M., D.A.R. and P.A.T.O.; validation: V.K.M., D.A.R. and P.A.T.O.; formal analysis: V.K.M., D.A.R. and P.A.T.O.; investigation: V.K.M., D.A.R. and P.A.T.O.; resources: V.K.M., D.A.R. and P.A.T.O.; data curation: V.K.M., D.A.R. and P.A.T.O.; writing—original draft preparation: V.K.M., D.A.R. and P.A.T.O.; writing—review and editing: V.K.M., D.A.R. and P.A.T.O.; visualization: V.K.M., D.A.R. and P.A.T.O.; supervision: V.K.M., D.A.R. and P.A.T.O.; project administration: V.K.M.; funding acquisition: V.K.M., D.A.R. and P.A.T.O. All authors have read and agreed to the published version of the manuscript.

Funding: Los Alamos National Laboratory is operated by Triad National Security, LLC, for the National Nuclear Security Administration of the U.S. Department of Energy under contract number 89233218NCA000001. PAT Olsson gratefully acknowledges financial support by the Swedish Research Council (grants no. 2016-04162 and 2022–04497), the Crafoord Foundation (grant no. 20150740) and the Swedish Knowledge Foundation (grant no. 20130022).

Data Availability Statement: The data required to reproduce these findings will be provided by the corresponding author upon reasonable request.

Acknowledgments: We acknowledge the support by the Institutional Computing Program at LANL, via the Center for Integrated Nanotechnologies, a DOE BES user facility, for computational resources. V. Mehta is very grateful for the discussions with J.I.A. Damian (Ignacio) from the European Spallation Source, which has significantly improved the quality of this paper. Parts of the computations were enabled by resources provided by the National Academic Infrastructure for Supercomputing in Sweden (NAISS) at the National Supercomputer Centre (NSC), Linköping University.

Conflicts of Interest: The authors declare no conflicts of interest.

Appendix A

NCrystal generated TSL plots for all zirconium hydride sub-stoichiometries investigated are given in Figure A1.

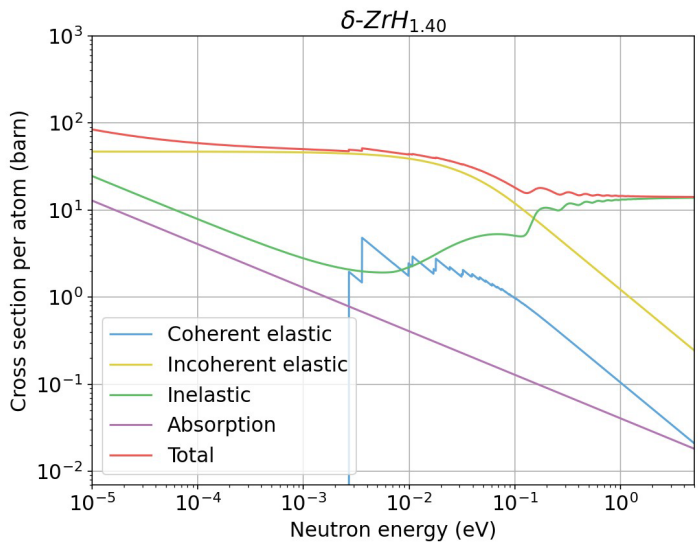

(**a**) δ-$ZrH_{1.40}$

Figure A1. *Cont.*

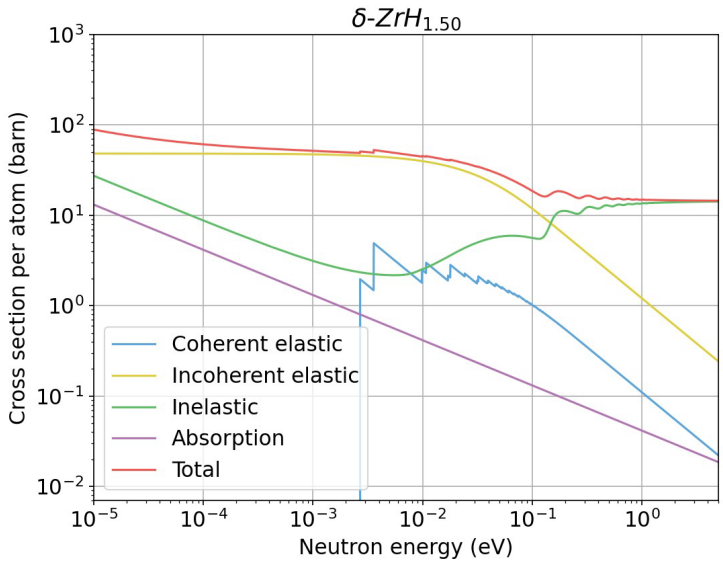

(**b**) δ-$ZrH_{1.50}$

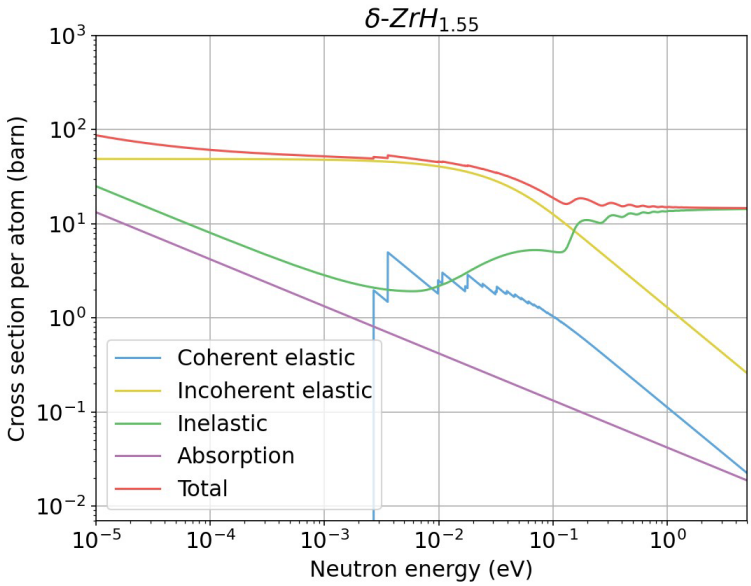

(**c**) δ-$ZrH_{1.55}$

Figure A1. *Cont.*

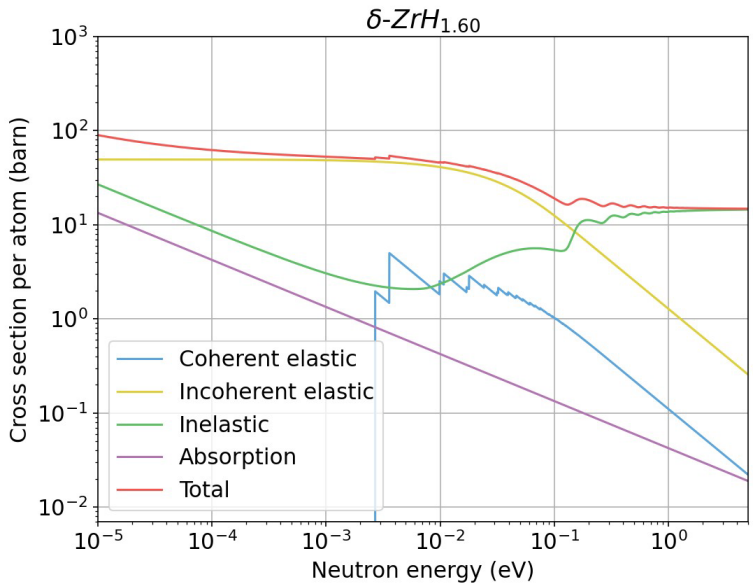

(**d**) δ-$ZrH_{1.60}$

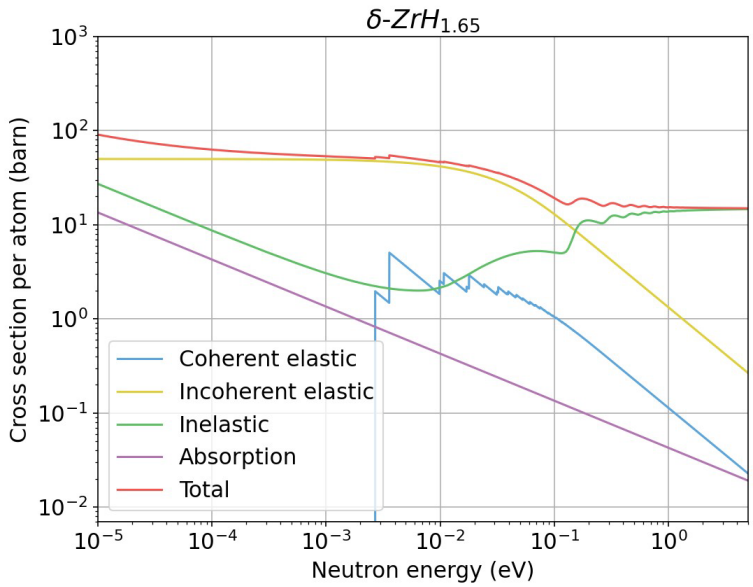

(**e**) δ-$ZrH_{1.65}$

Figure A1. *Cont.*

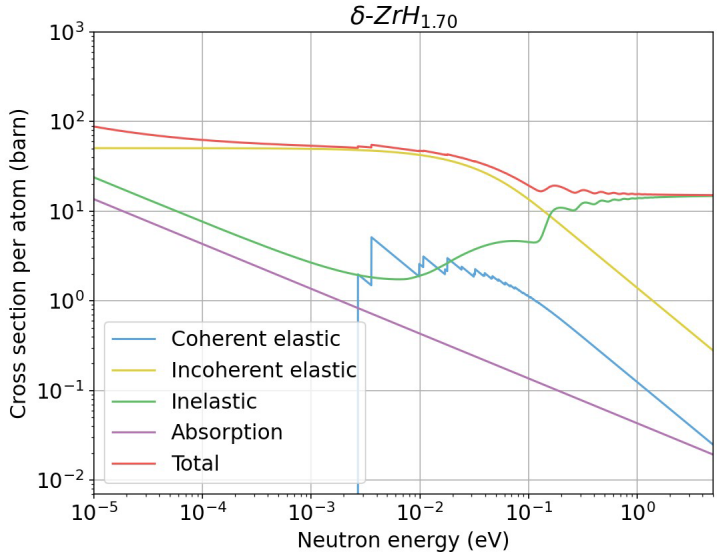

(**f**) δ-ZrH$_{1.70}$

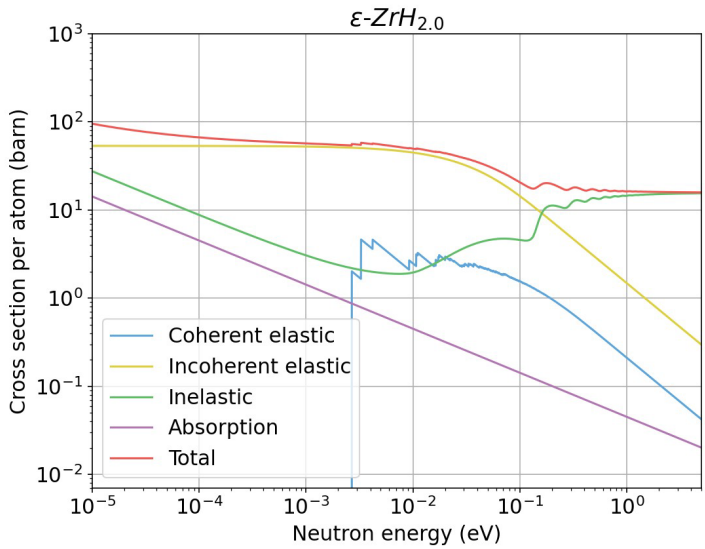

(**g**) ϵ-ZrH$_{2.00}$

Figure A1. Detailed thermal scattering law profiles for all stoichiometries evaluated in this work. Plots generated using NCrystal. Cross sections are on a per atom basis as defaulted by NCrystal.

References

1. McClure, P.R.; Poston, D.I.; Gibson, M.A.; Mason, L.S.; Robinson, R.C. Kilopower Project: The KRUSTY Fission Power Experiment and Potential Missions. *Nucl. Technol.* **2020**, *206*, S1–S12. [CrossRef]
2. Poston, D.I.; Gibson, M.A.; Godfroy, T.; McClure, P.R. KRUSTY Reactor Design. *Nucl. Technol.* **2020**, *206*, 13–30. [CrossRef]
3. Gibson, M.A.; Poston, D.I.; McClure, P.R.; Sanzi, J.L.; Godfroy, T.J.; Briggs, M.H.; Wilson, S.D.; Schifer, N.A.; Chaiken, M.F.; Lugasy, N. Heat Transport and Power Conversion of the Kilopower Reactor Test. *Nucl. Technol.* **2020**, *206*, 31–42. [CrossRef]
4. McClure, P.R.; Poston, D.I.; Clement, S.D.; Restrepo, L.; Miller, R.; Negrete, M. KRUSTY Experiment: Reactivity Insertion Accident Analysis. *Nucl. Technol.* **2020**, *206*, S43–S55. [CrossRef]
5. Sanchez, R.; Grove, T.; Hayes, D.; Goda, J.; McKenzie, G.; Hutchinson, J.; Cutler, T.; Bounds, J.; Walker, J.; Myers, W.; et al. Kilowatt Reactor Using Stirling TechnologY (KRUSTY) Component-Critical Experiments. *Nucl. Technol.* **2020**, *206*, 56–67. [CrossRef]
6. Grove, T.; Hayes, D.; Goda, J.; McKenzie, G.; Hutchinson, J.; Cutler, T.; Bounds, J.; Walker, J.; Myers, W.; Sanchez, R. Kilowatt Reactor Using Stirling TechnologY (KRUSTY) Cold Critical Measurements. *Nucl. Technol.* **2020**, *206*, S68–S77. [CrossRef]
7. Poston, D.I.; Gibson, M.A.; McClure, P.R.; Sanchez, R.G. Results of the KRUSTY Warm Critical Experiments. *Nucl. Technol.* **2020**, *206*, S78–S88. [CrossRef]
8. Poston, D.I.; Gibson, M.A.; Sanchez, R.G.; McClure, P.R. Results of the KRUSTY Nuclear System Test. *Nucl. Technol.* **2020**, *206*, S89–S117. [CrossRef]

9. Mehta, V.K.; McClure, P.; Kotlyar, D. Selection of a Space Reactor Moderator Using Lessons Learned from SNAP and ANP Programs. In Proceedings of the AIAA Propulsion and Energy 2019 Forum, Indianapolis, IN, USA, 19–22 August 2019.
10. Voss, S.S. *Topaz II System Description*; No. LA-UR--94-4; Los Alamos National Lab.: Los Alamos, NM, USA, 1994.
11. Olander, D. Nuclear fuels–present and future. *J. Nucl. Mater.* **2009**, *389*, 1–22. [CrossRef]
12. Lillie, A.F.; McClelland, D.T.; Roberts, W.J.; Walter, J.H. *Zirconium Hydride Fuel Element Performance Characteristics*; No. AI-AEC--13084; Atomics International Division: Los Angeles, CA, USA, 1973.
13. Gates, J.; Denig, A.; Ahmed, R.; Mehta, V.; Kotlyar, D. Low-enriched cermet-based fuel options for a nuclear thermal propulsion engine. *Nucl. Eng. Des.* **2018**, *331*, 313–330. [CrossRef]
14. Johnson, J.; Patterson, M.W.; Wagner, A.R. *MARVEL Fuel Fabrication Strategy*; No. INL/RPT-22-66550-Rev000; Idaho National Lab. (INL): Idaho Falls, ID, USA, 2022.
15. Mehta, V.K.; Armstrong, J.; Rao, D.V.; Kotlyar, D. Capturing multiphysics effects in hydride moderated microreactors using MARM. *Ann. Nucl. Energy* **2022**, *172*, 109067. [CrossRef]
16. Trellue, H.R.; Long, A.M.; Luther, E.P.; Carver, D.T.; Mehta, V.K. Effects of Hydrogen Redistribution at High Temperatures in Yttrium Hydride Moderator Material. *JOM* **2021**, *73*, 3513–3518. [CrossRef]
17. Hawley, J.P.; Johnson, R.A. *SNAP 10A FS-3 Reactor Performance*; No. NAA-SR-11397; Atomics International Division: Canoga Park, CA, USA, 1966.
18. Taylor, C.; Smith, T.; Hahn, M.; Torres, J.; Tegtmeier, E.; Nizolek, T.; Bohn, K.; Emberley, C.; Shivprasad, A.; Widgeon-Paisner, S.; et al. *Properties of Uranium-Zirconium Hydride Moderated Nuclear Fuel Synthesized by Powder Metallurgy*; Technical Report LA-UR-22-29969; Los Alamos National Laboratory: Los Alamos, NM, USA, 2022.
19. Zuzek, E.; Abriata, J.; San-Martin, A.; Manchester, F. *Phase Diagrams of Binary Hydrogen Alloys*; ASM International: Materials Park, OH, USA, 2000; pp. 309–310.
20. Wormald, J.; Zerkle, M.; Holmes, J. Generation of the TSL for Zirconium Hydrides from Ab Initio Methods. *J. Nucl. Eng.* **2021**, *2*, 105–113. [CrossRef]
21. Zu, T.; Tang, Y.; Wang, L.; Cao, L.; Wu, H. Thermal scattering law data generation for hydrogen bound in zirconium hydride based on the phonon density of states from first-principles calculations. *Ann. Nucl. Energy* **2021**, *161*, 108489. [CrossRef]
22. El Barbari, M.; El Bardouni, T.; El Yaakoubi, H.; Boulaich, Y.; Lahdour, M.; Ziani, H.; Berriban, I. First principles calculation for generating new thermal neutron scattering data for Zirconium hydride. *Appl. Radiat. Isot.* **2022**, *187*, 110313. [CrossRef]
23. Švajger, I.; Fleming, N.C.; Laramee, B.; Noguere, G.; Hawari, A.I.; Snoj, L.; Trkov, A. Thermal Scattering Law Data for Zirconium Hydride from First-Principles. In Proceedings of the International Conference Nuclear Energy for New Europe, Bled, Slovenia, 6–9 September 2021; p. 307.
24. Fleming, N.C.; Manring, C.A.; Laramee, B.K.; Crozier, J.P.; Lee, E.; Hawari, A.I. *FLASSH* 1.0: Thermal Scattering Law Evaluation and Cross Section Generation. *EPJ Web Conf.* **2023**, *284*, 17007. [CrossRef]
25. Baroni, S.; de Gironcoli, S.; Corso, A.D.; Giannozzi, P. Phonons and related crystal properties from density-functional perturbation theory. *Rev. Mod. Phys.* **2001**, *73*, 515–562. [CrossRef]
26. Kresse, G.; Furthmüller, J. Efficient iterative schemes for ab initio total-energy calculations using a plane-wave basis set. *Phys. Rev. B* **1996**, *54*, 11169. [CrossRef]
27. Kresse, G.; Furthmüller, J. Efficiency of ab-initio total energy calculations for metals and semiconductors using a plane-wave basis set. *Comput. Mater. Sci.* **1996**, *6*, 15–50. [CrossRef]
28. Togo, A. First-principles Phonon Calculations with Phonopy and Phono3py. *J. Phys. Soc. Jpn.* **2023**, *92*, 012001. [CrossRef]
29. Togo, A.; Chaput, L.; Tadano, T.; Tanaka, I. Implementation strategies in phonopy and phono3py. *J. Phys. Condens. Matter* **2023**, *35*, 353001. [CrossRef] [PubMed]
30. Zu, T.; Xu, J.; Tang, Y.; Bi, H.; Zhao, F.; Cao, L.; Wu, H. NECP-Atlas: A new nuclear data processing code. *Ann. Nucl. Energy* **2019**, *123*, 153–161. [CrossRef]
31. Gonze, X.; Jollet, F.; Araujo, F.A.; Adams, D.; Amadon, B.; Applencourt, T.; Audouze, C.; Beuken, J.M.; Bieder, J.; Bokhanchuk, A.; et al. Recent developments in the ABINIT software package. *Comput. Phys. Commun.* **2016**, *205*, 106–131. [CrossRef]
32. Haeck, W.; Conlin, J.L.; McCartney, A.P.; Kahler, A.C., III. *NJOY2016 Updates for ENDF/B-VIII. 0*; No. LA-UR-18-22676; Los Alamos National Lab. (LANL): Los Alamos, NM, USA, 2018.
33. Ramić, K.; Damian, J.I.M.; Kittelmann, T.; Di Julio, D.D.; Campi, D.; Bernasconi, M.; Gorini, G.; Santoro, V. NJOY+NCrystal: An open-source tool for creating thermal neutron scattering libraries with mixed elastic support. *Nucl. Instrum. Methods Phys. Res. Sect. A Accel. Spectrometers Detect. Assoc. Equip.* **2022**, *1027*, 166227. [CrossRef]
34. Kulesza, J.A.; Adams, T.R.; Armstrong, J.C.; Bolding, S.R.; Brown, F.B.; Bull, J.S.; Burke, T.P.; Clark, A.R.; Forster, R.A.A., III; Giron, J.F.; et al. *MCNP® Code Version 6.3. 0 Theory & User Manual*; No. LA-UR-22-30006; Los Alamos National Lab. (LANL): Los Alamos, NM, USA, 2022.
35. Yamanaka, S.; Yamada, K.; Kurosaki, K.; Uno, M.; Takeda, K.; Anada, H.; Matsuda, T.; Kobayashi, S. Characteristics of zirconium hydride and deuteride. *J. Alloys Compd.* **2002**, *330*, 99–104. [CrossRef]
36. Bowman, R.C., Jr.; Craft, B.D.; Cantrell, J.S.; Venturini, E.L. Effects of thermal treatments on the lattice properties and electronic structure of ZrHx. *Phys. Rev. B* **1985**, *31*, 5604. [CrossRef]
37. Beck, R.L. Thermophysical properties of zirconium hydride. *ASM Trans. Q.* **1962**, *55*, 556–564.

38. Moore, K.; Young, W. Phase studies of the Zr-H system at high hydrogen concentrations. *J. Nucl. Mater.* **1968**, *27*, 316–324. [CrossRef]
39. Hawari, A.I.; Al-Qasir, I.I.; Gillette, V.H.; Wehring, B.W.; Zhou, T. Ab initio generation of thermal neutron scattering cross sections. In Proceedings of the PHYSOR 2003, Chicago, IL, USA, 25–29 April 2004.
40. Hawari, A. Modern Techniques for Inelastic Thermal Neutron Scattering Analysis. *Nucl. Data Sheets* **2014**, *118*, 172–175. [CrossRef]
41. Rahman, A.; Mandell, M.J.; McTague, J.P. Molecular dynamics study of an amorphous Lennard-Jones system at low temperature. *J. Chem. Phys.* **1976**, *64*, 1564–1568. [CrossRef]
42. Wormald, J.; Hawari, A. Generation of phonon density of states and thermal scattering law using ab initio molecular dynamics. *Prog. Nucl. Energy* **2017**, *101*, 461–467. [CrossRef]
43. Wormald, J.; Hawari, A.I. Thermal neutron scattering law calculations using ab initio molecular dynamics. *EPJ Web Conf.* **2017**, *146*, 13002. [CrossRef]
44. Blöchl, P.E. Projector augmented-wave method. *Phys. Rev. B* **1994**, *50*, 17953–17979. [CrossRef] [PubMed]
45. Kresse, G.; Joubert, D. From ultrasoft pseudopotentials to the projector augmented-wave method. *Phys. Rev. B* **1999**, *59*, 1758–1775. [CrossRef]
46. Perdew, J.P.; Burke, K.; Ernzerhof, M. Generalized gradient approximation made simple. *Phys. Rev. Lett.* **1996**, *77*, 3865–3868. [CrossRef]
47. Monkhorst, H.J.; Pack, J.D. Special points for Brillouin-zone integrations. *Phys. Rev. B* **1976**, *13*, 5188–5192. [CrossRef]
48. Nosé, S.A. unified formulation of the constant temperature molecular dynamics methods. *J. Chem. Phys.* **1984**, *81*, 511–519. [CrossRef]
49. Nosé, S.A. Molecular dynamics method for simulations in the canonical ensemble. *Mol. Phys.* **1984**, *52*, 255–268. [CrossRef]
50. Hoover, W.G. Canonical dynamics: Equilibrium phase-space distributions. *Phys. Rev. A* **1985**, *31*, 1695–1697. [CrossRef]
51. Evans, D.J.; Holian, B.L. The Nosé–Hoover thermostat. *J. Chem. Phys.* **1985**, *83*, 4069–4074. [CrossRef]
52. Hellman, O.; Abrikosov, I.A.; Simak, S.I. Lattice dynamics of anharmonic solids from first principles. *Phys. Rev. B* **2011**, *84*, 180301. [CrossRef]
53. Hellman, O.; Abrikosov, I.A. Temperature-dependent effective third-order interatomic force constants from first principles. *Phys. Rev. B* **2013**, *88*, 144301. [CrossRef]
54. Hellman, O.; Steneteg, P.; Abrikosov, I.A.; Simak, S.I. Temperature dependent effective potential method for accurate free energy calculations of solids. *Phys. Rev. B* **2013**, *87*, 104111. [CrossRef]
55. Olsson, P.A.T.; Massih, A.; Blomqvist, J.; Holston, A.-M.A.; Bjerkén, C. Ab initio thermodynamics of zirconium hydrides and deuterides. *Comput. Mater. Sci.* **2014**, *86*, 211–222. [CrossRef]
56. Squires, G.L.; Leslie, G. *Introduction to the Theory of Thermal Neutron Scattering*; Courier Corporation: North Chelmsford, MA, USA, 1996.
57. Bell, G.I.; Glasstone, S. *Nuclear Reactor Theory*; No. TID-25606; US Atomic Energy Commission: Washington, DC, USA, 1970.
58. Brown, D.A.; Chadwick, M.B.; Capote, R.; Kahler, A.C.; Trkov, A.; Herman, M.W.; Sonzogni, A.A.; Danon, Y.; Carlson, A.D.; Dunn, M.; et al. ENDF/B-VIII. 0: The 8th major release of the nuclear reaction data library with CIELO-project cross sections, new standards and thermal scattering data. *Nucl. Data Sheets* **2018**, *148*, 1–142. [CrossRef]
59. Zerkle, M.; Holmes, J. A thermal neutron scattering law for yttrium hydride. *EPJ Web Conf.* **2017**, *146*, 13005. [CrossRef]
60. Mehta, V.K.; Cooper, M.W.; Wilkerson, R.B.; Kotlyar, D.; Rao, D.V.; Vogel, S.C. Evaluation of Yttrium Hydride (δ-YH2-*x*): Thermal Neutron Scattering Laws and Thermophysical Properties. *Nucl. Sci. Eng.* **2021**, *195*, 563–577. [CrossRef]
61. Cai, X.-X.; Kittelmann, T. NCrystal: A library for thermal neutron transport. *Comput. Phys. Commun.* **2020**, *246*, 106851. [CrossRef]
62. Trkov, A.; Brown, D.A. *ENDF-6 Formats Manual: Data Formats and Procedures for the Evaluated Nuclear Data Files*; CSWEG Document ENDF-102, BNL-203218-2018-INRE; Brookhaven National Laboratory: Upton, NY, USA, 2018.
63. Couch, J.G.; Harling, O.K.; Clune, L.C. Structure in the Neutron Scattering Spectra of Zirconium Hydride. *Phys. Rev. B* **1971**, *4*, 2675–2681. [CrossRef]
64. Evans, A.C.; Timms, D.N.; Mayers, J.; Bennington, S.M. Neutron-scattering study of the impulse approximation in ZrH_2. *Phys. Rev. B* **1996**, *53*, 3023. [CrossRef]
65. Flotow, H.E.; Osborne, D.W. Heat Capacities and Thermodynamic Functions of ZrH_2 and ZrD_2 from 5 to 350 °K and the Hydrogen Vibration Frequency in ZrH_2. *J. Chem. Phys.* **1961**, *34*, 1418–1425. [CrossRef]
66. Whittemore, W.L. *Neutron Interactions in Zirconium Hydride*; GA-4490; General Atomics: San Diego, CA, USA, 1964.
67. Schmidt, U. Untersuchung derWasserstoff- und Deuteriumschwingungen in Metallhydriden, -Hydrodeuteriden und -Deuteriden Mittles Totaler Neutronen-Wirkunsquerschnitte. *ATKE* **1967**, *12*, 385.